Energy Conversion and Management 99 (2015) 346–358

Contents lists available at ScienceDirect

Energy Conversion and Management

journal homepage: www.elsevier.com/locate/enconman

Multi-objective optimization of a multi-step solar-driven Brayton plant

S. Sánchez-Orgaz [a], M. Pedemonte [b], P. Ezzatti [b], P.L. Curto-Risso [c], A. Medina [d,*], A. Calvo Hernández [d]

[a] ETSII de Béjar, Universidad de Salamanca, 37700 Béjar, Spain
[b] Instituto de Computación, Universidad de la República, 11300 Montevideo, Uruguay
[c] Instituto de Ingeniería Mecánica y Producción Industrial, Universidad de la República, 11300 Montevideo, Uruguay
[d] Departamento de Física Aplicada, Universidad de Salamanca, 37008 Salamanca, Spain

ARTICLE INFO

Article history:
Received 10 February 2015
Accepted 24 April 2015

Keywords:
Brayton plant
Thermodynamic model
Multi-objective optimization
Evolutionary algorithm
Optimal design parameters

ABSTRACT

A multi-objective and multi-parametric optimization analysis is presented for a recuperative multi-step solar-driven Brayton thermosolar plant. The analysis is done over a thermodynamic analytical model that incorporates all the losses observed in real plants, from the heat engine itself and from the solar subsystem. The model allows to consider several compression–expansion stages. The overall system efficiency and the power output were taken as objective functions. The Pareto Front of the system is obtained by considering possible fluctuations in all the involved parameters. This study allows to discern the significant design variables. Then, the exact Pareto Fronts were calculated, by taking as variables only those parameters, and building an appropriate grid. Several configurations (ideal and realistic, with single stage or multi-step compression–expansion processes) were analyzed and multi-criteria decision making procedures applied in order to obtain physical insights from the results. It was shown the importance of electing an appropriate conducting gas, and adequate values of the global pressure and temperature ratios. This study could constitute an interesting guideline for the design of future generations of plants of this type, that are now at the research and developing stage.

1. Introduction

A promising technology in electric energy generation is the utilization of concentrated solar energy as energy input for a Brayton type gas turbine. This is usually done in central receiver solar installations.These plants can contribute to produce clean energy with a reduced consumption of fossil fuels. Several projects in the last years [1–3] have shown their feasibility as well as the necessity to optimize the design of future facilities in order to be commercially interesting. Up to date production costs are still high and efficiencies require substantial improvement. From this point of view thermodynamic analyses of these systems can play an interesting role. They provide a global perspective of the plant and the main flaw processes maybe identified and optimized. There exist in the literature several works relative to the model and optimization of solar systems working in different thermodynamic cycles as Carnot, Ericsson, Braysson, and Stirling [4–6] or Brayton [7–14]. In all of these works a pure thermodynamic model is proposed for the considered cycle. The model starts from the principles of Classical Reversible Thermodynamics and then several losses (irreversibility) sources are considered in order to reproduce the behavior of real systems. In this way analytical equations for the system performance are obtained and, eventually an optimization analysis can be performed. Usually, one or two parameters are considered for optimization once the reminder are considered as fixed. This is elucidating from the theoretical viewpoint. Nevertheless, the main inconvenience of this kind of studies is that they only provide partial conclusions for the optimization of real systems, because in them complex relationships between variables make that efficiency or other output records depend simultaneously on several variables in a non trivial way. Moreover, in this procedure it is not possible to simultaneously optimize two or more objective functions.

Nevertheless, there exists another kind of approximation. It relies on the combination of thermodynamic analysis with multi-objective and multi-parametric optimization techniques [15]. In this way the main advantages of thermodynamic analyses are maintained: identification of the main losses sources, analytical formulation of expressions for efficiency, power or any other objective function, easy checking of the sensitivity of the system to a particular parameter, reduced computational costs, etc. And at the same time it is possible to obtain reliable information on the system optimization because a simultaneous study on two or more objective functions including the influence of several

* Corresponding author.
E-mail addresses: susan@usal.es (S. Sánchez-Orgaz), mpedemon@fing.edu.uy (M. Pedemonte), pezzatti@fing.edu.uy (P. Ezzatti), pcurto@fing.edu.uy (P.L. Curto-Risso), amd385@usal.es (A. Medina), anca@usal.es (A. Calvo Hernández).

http://dx.doi.org/10.1016/j.enconman.2015.04.077
0196-8904/

Nomenclature

A_a	aperture area of the collector
A_r	absorber area of the collector
a_c	isentropic compressor pressure ratio
a_t	isentropic turbine pressure ratio
C	solar collector concentration ratio
C_w	heat capacity rate of the working fluid
G	solar irradiance
I-conf.	ideal plant configuration
M_1	radiation heat loss coefficient for the solar collector
M_2	effective convection and conduction loss coefficient for the solar collector
N_C	number of compression stages
N_T	number of expansion stages
N	number of compression and expansion stages assumed equal
n_{PF}	number of points of the Pareto Front
NRR-conf.	non-regenerative realistic plant configuration
P	power output
$\overline{P}$	adimensional power output
$\lvert\dot{Q}_H\rvert$	total heat absorbed by the working fluid
$\lvert\dot{Q}_L\rvert$	heat release from the working fluid to the ambient
$\lvert\dot{Q}_s\rvert$	heat input in the solar collector
r_p	overall pressure ratio
R-conf.	realistic plant configuration
T_H	working temperature of the solar collector
T_L	ambient temperature
T_1	compressors inlet temperature
T_3	turbines inlet temperature
U_L	convective losses of the solar collector
α	effective emissivity
ϵ_H	solar collector heat exchanger efficiency
ϵ_c	isentropic efficiency of the compressors
ϵ_L	cold side heat exchanger efficiency
ϵ_r	regenerator effectiveness
ϵ_t	isentropic efficiency of the turbines
γ	adiabatic coefficient of the working fluid
ξ	heat leakage coefficient
ρ_H	irreversibilities due to pressure drops in the heat input
ρ_L	irreversibilities due to pressure drops in the heat release
η	overall thermal efficiency
η_s	solar collector efficiency
η_0	effective transmittance–absorptance product
σ	Stefan–Boltzmann constant
τ	temperature ratio associated to the solar collector

variables can be performed. This approach has been applied in the last years to thermodynamic cycles with conventional or solar heat input like Stirling [16,17], Ericsson [18], Brayton [8,19–22], and Braysson [23]. Also recently a paper by Ahmadi et al. [24] deals with the analysis of a solar-driven Brayton cycle from a thermodynamic model developed by our group [12,13,25], but significant information relative to the number of compression–expansion stages, the values taken for the fixed parameters, and the possible links among the variables that were considered as free variables, was not provided.

In this work our objective is to perform a detailed multi-objective optimization study based upon a thermodynamic model previously developed by us of a solar-driven gas turbine plant. The model describes a multi-stage recuperative Brayton turbine receiving the heat input from a concentrating solar collector. It incorporates the main irreversibility terms in this type of systems, both from the solar subsystem and the turbine itself: heat losses in the collector, pressure losses in the heat absorption from the turbine, turbines and compressor non-isentropic processes, losses in the recuperator and in all the heat exchangers. By using an evolutionary algorithm and taking as objective functions the overall plant efficiency and the power output, we obtained the Pareto Front by considering, in principle, all the main system parameters as free variables. After identifying the relevant ones, the exact Pareto Front was calculated by a thorough evaluation of the search space, keeping the non-relevant parameters as fixed and using a fine discretization for the others. Several plant configurations, with a different number of compression–expansion stages were considered and the working intervals for the free variables were carefully surveyed. Moreover, the representative points of the Pareto Front were analyzed in different situations: an ideal configuration with minimized losses, a non-recuperative configuration, and a realistic layout with parameters taken from existing real installations. We emphasize the main novelties of this work with respect to previous ones: the exact Pareto Front is obtained after a systematic search of the relevant system parameters, several plant configurations within a multi-step compression–expansion scheme are investigated, and also ideal and non-recuperative configurations are analyzed.

2. Thermodynamic model of a Brayton-solar cycle

Our model for an irreversible solar-driven multi-step Brayton heat engine is depicted in Fig. 1(a). The analytical model incorporates an arbitrary number of turbines and compressors coupled to a solar collector for which heat losses from convection, conduction, and radiation are considered, (for more details see [12,13]). The overall efficiency of the coupled system is given by: $\eta = \eta_h \eta_s$. η_h represents the thermal efficiency of the heat engine, $\eta_h = \frac{P}{|\dot{Q}_H|} = 1 - \frac{|\dot{Q}_L|}{|\dot{Q}_H|}$, and η_s is the efficiency of the solar collector, $\eta_s = \frac{|\dot{Q}_H|}{|\dot{Q}_s|}$, where P is the net power output of the cycle, $P = |\dot{Q}_H| - |\dot{Q}_L|$, $|\dot{Q}_H|$ is the total heat input absorbed by the working fluid, $|\dot{Q}_L|$ is the heat released to the surroundings, and $|\dot{Q}_s|$ is the solar heat input in the solar collector.

2.1. Efficiency of the solar collector

A concentrating collector is considered with the aim to get a higher efficiency for the overall system. It is well-known that at low and intermediate temperatures, heat losses in the solar collector are essentially associated to conduction and convection and that at high enough temperatures radiation losses are dominant [26]. In this model the useful energy delivered to the heat engine is given by, $|\dot{Q}_H| = |\dot{Q}_r - \dot{Q}_\ell|$, where $|\dot{Q}_r| = \eta_0 G A_a$ represents the energy per unit of time transmitted to the receiver and $|\dot{Q}_\ell|$ the losses by conduction, convection, (both proportional to the first power of temperature) and radiation (proportional to T^4), $|\dot{Q}_\ell| = A_r \alpha \sigma \left(T_H^4 - T_L^4\right) - A_r U_L (T_H - T_L)$. η_0 is the effective transmittance–absorptance product (optical efficiency), G is the solar irradiance, A_a and A_r are respectively the aperture and absorber areas, α is the effective emissivity, σ is the Stefan–Boltzmann constant and U_L the overall conduction and convection heat loss coefficient of the solar collector [27,28]. The energy per unit time received in the aperture area is $|\dot{Q}_s| = G A_a$.

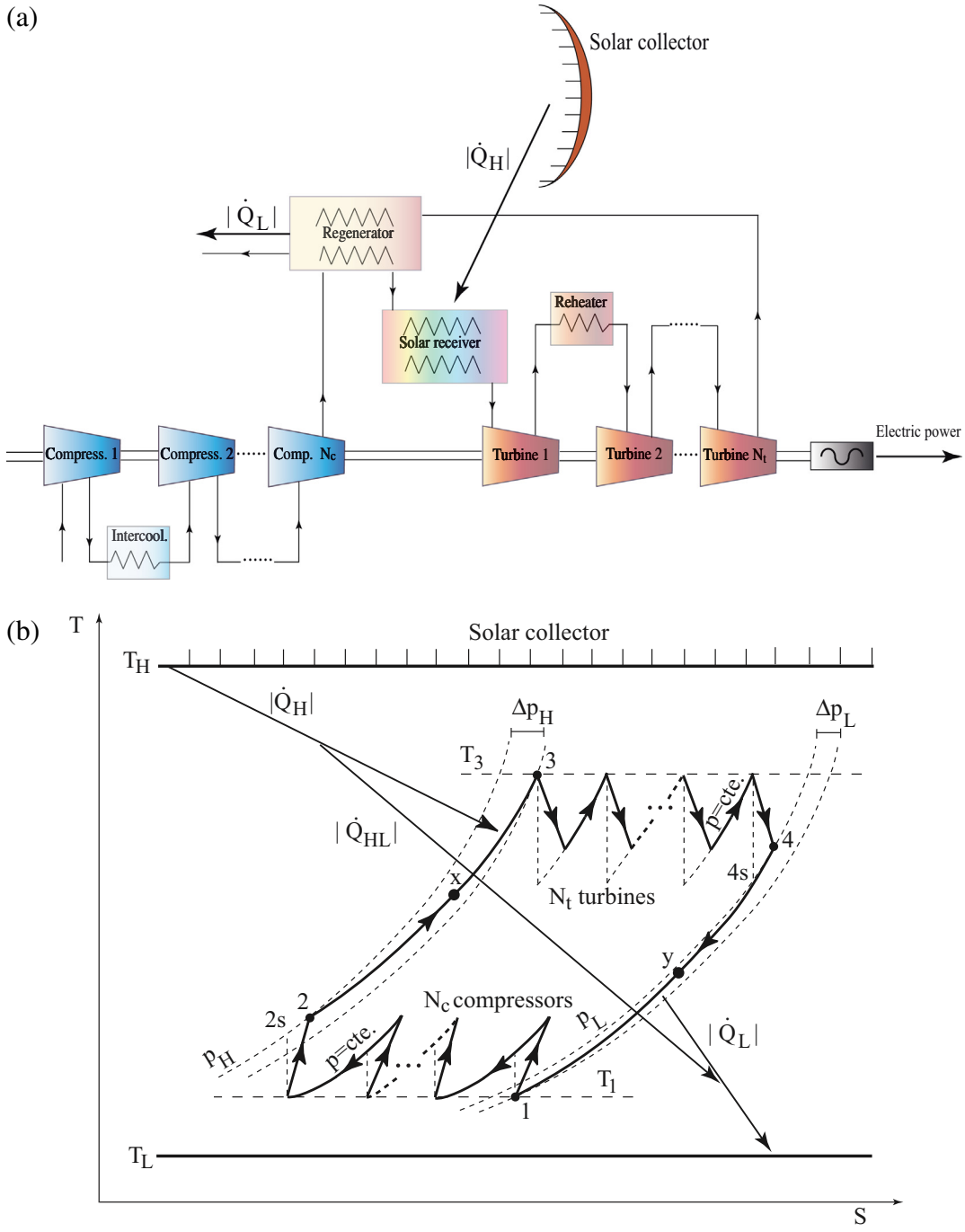

Fig. 1. (a) Scheme of the solar-driven Brayton plant considered. It incorporates a recuperator and an arbitrary number of turbines and compressors with the corresponding intercoolers and reheaters. (b) $T-S$ diagram of the thermodynamic cycle [13].

Thus, the efficiency of the solar collector (see [26,29] for details) reads as:

$$\eta_s = \eta_0\left[1 - M_1(\tau^4 - 1) - M_2(\tau - 1)\right], \tag{1}$$

where M_1 and M_2 are two losses parameters defined as: $M_1 = \alpha\sigma T_L^4/(\eta_0 GC)$ and $M_2 = U_L T_L/(\eta_0 GC)$, $\tau = T_H/T_L$ is the heat reservoirs temperature ratio and $C = A_a/A_r$ the concentration ratio [12,13].

2.2. Irreversible multi-step Brayton heat engine

This model for the multi-step Brayton heat engine [25] has been validated and compared with experimental facilities in [29]. We consider irreversibilities for turbines and compressors, pressure drops in the heat input and heat release, heat leakage, and non-ideal couplings of the working fluid with the external heat reservoirs. It is considered as working fluid and ideal gas with temperature independent heat capacities and adiabatic constant, γ, and flowing in stationary conditions. Here, we briefly summarize the most important steps in the thermodynamic cycle (see Fig. 1(b)):

1. The working fluid is compressed from the initial state 1 by means of N_c non-adiabatic compressors and $N_c - 1$ isobaric intercoolers. All the compressors are assumed to have the same isentropic efficiency ϵ_c and the same inlet temperature T_1 [12].

2. The gas is pre-heated after state 2 in a regenerative heat exchanger to state X, that has an effectiveness ϵ_r. A non-regenerative cycle corresponds to $\epsilon_r = 0$ and ideal or limit regeneration to $\epsilon_r = 1$. After X the working fluid is heated up with the useful heat released from the solar collector to T_3, that is the turbine inlet temperature. The losses in this heat input processes are accounted by $\epsilon_H = (T_X - T_3)/(T_X - T_H)$. The overall heating process from state 2 to 3 is considered as non-isobaric, with a pressure drop quantified by ρ_H ($\rho_H = 1$ corresponds to a zero pressure decay) [30].
3. Afterwards reaching the maximum temperature in the cycle, T_3, the working fluid is expanded by means of N_t non-adiabatic turbines and $N_t - 1$ isobaric reheaters. The efficiency of all turbines is the same, ϵ_t and the inlet temperature for all of them is T_3.
4. The heat release process between state 4 and 1 is divided into two parts, a cooling from 4 to Y through the regenerative heat exchanger and a following cooling from T_Y to T_1. The effectiveness of this irreversible heat transfer is denoted as ϵ_L. A global pressure decay quantified by ρ_L ($\rho_L = 1$ corresponds to a zero pressure decay) is considered during the entire cooling process.

The isentropic compressor and turbine pressure ratios, $a_t = T_3/T_{4s}$ and $a_c = T_{2s}/T_1 = r_p^{(\gamma-1)/\gamma}$ where $r_p = P_2/P_1$ is the global pressure ratio, can be related through the parameters accounting for the pressure drops in the $2 \to 3$ heating and $4 \to 1$ cooling processes as $a_t = a_c\rho_H\rho_L$.

Heat is provided to the system along the process $X \to 3$ (in absence of regeneration from $2 \to 3$) and along the $N_t - 1$ reheating processes between turbines and can be expressed as [25]:

$$|\dot{Q}_H| = C_w T_L \left\{ \epsilon_H \left[\tau - Z_c(1-\epsilon_r)\frac{T_1}{T_L} - \epsilon_r Z_t \frac{T_3}{T_L} \right] + \epsilon_t (N_t - 1)\left(1 - a_t^{-1/N_t}\right)\frac{T_3}{T_L} + \xi(\tau - 1) \right\} \quad (2)$$

where C_w is the heat capacity rate of the working fluid,

$$Z_c = 1 + \frac{a_c^{1/N_c} - 1}{\epsilon_c}$$

$$Z_t = 1 - \epsilon_t\left(1 - a_t^{-1/N_t}\right) \quad (3)$$

and

$$\frac{T_1}{T_L} = \frac{\epsilon_L + (1-\epsilon_L)(1-\epsilon_r)Z_t\left(\frac{T_3}{T_L}\right)}{1 - (1-\epsilon_L)\epsilon_r Z_c} \quad (4)$$

$$\frac{T_3}{T_L} = \frac{\tau\epsilon_H[1-(1-\epsilon_L)\epsilon_r Z_c] + \epsilon_L(1-\epsilon_H)(1-\epsilon_r)Z_c}{[1-(1-\epsilon_L)\epsilon_r Z_c][1-(1-\epsilon_H)\epsilon_r Z_t] - (1-\epsilon_H)(1-\epsilon_L)(1-\epsilon_r)^2 Z_t Z_c} \quad (5)$$

The term $\xi(\tau - 1)$ in Eq. (2) represents the linear heat leakage. $\xi = C_i/C_w$ where C_i is the internal conductance of the power plant [31,32].

Because of the existence of an irreversible regenerator, effective heat release is associated to the process $Y \to 1$ and to the cooling processes from the $N_c - 1$ intercoolers between the compressors. The heat release is given by:

$$|\dot{Q}_L| = C_w T_L \left\{ \epsilon_L \left[-1 + Z_t(1-\epsilon_r)\frac{T_3}{T_L} + \epsilon_r Z_c \frac{T_1}{T_L} \right] + \frac{1}{\epsilon_c}(N_c - 1)(a_c^{1/N_c} - 1)\frac{T_1}{T_L} + \xi(\tau - 1) \right\} \quad (6)$$

where $Z_c, Z_t, T_1/T_L$ and T_3/T_L are given by Eqs. (3)–(5). Eqs. (2) and (6) for the heat input and heat release allow to obtain the efficiency of the Brayton heat engine, η_h, and subsequently the overall plant efficiency through $\eta = \eta_h\eta_s$. This efficiency and any other output record are functions of several geometrical parameters that characterize the shape and size of the cycle, and other parameters that quantify the internal and external irreversibilities affecting all the plant subsystems.

Previous studies have shown the influence of some of these parameters on the overall plant efficiency. For instance, the dependence of η with the temperature ratio, τ and the pressure ratio, r_p was analyzed in [12,13]. The behavior is depicted in Fig. 2: the solar collector efficiency, η_s, is a monotonically decreasing function with increasing τ because heat losses are larger for higher working temperature for the collector. On the contrary, the heat engine thermodynamic efficiency, η_h, increases as the ratio between external heat sources increases. So, the overall efficiency, η, that is the simple product of both efficiencies, always presents a parabolic-like shape with a maximum as a function of τ. This makes η an optimizable function in terms of τ. This figure also allows to understand the plausible interval of values for τ. Its minimum value is associated to the heat engine, which efficiency becomes 0 for small values of τ and its maximum value is associated to the solar subsystem that leads to negative values of η_s when temperatures are high and heat losses in the collector become too large. The lowest value of τ depends on all the parameters affecting the heat engine efficiency (pressure ratio and losses terms), roughly it is between $\tau = 2.5$ and $\tau = 3.5$. The upper limit only depends on the particularities of the solar subsystem. For the parameters considered in the figure, $\tau = 4.4$.

Additionally, in previous works, it was shown that for a simple one-compressor one-turbine plant, the effect of the regenerator is subtle: only for low enough pressure ratios maximum overall efficiency increases with a larger regenerator effectiveness, ϵ_r [13]. This is a direct consequence of the coupling of the solar and the Brayton subsystems and can be explained from Fig. 2. It is a well-known result from textbooks that regeneration in a Brayton recuperative cycle is only effective for high enough temperature ratios. These temperature ratios increase with r_p. This is shown in the insets of the figure. In the inset of the upper panel, η_h is higher for high values of ϵ_r from about $\tau = 2.8$. When making the product $\eta = \eta_h\eta_s$ to obtain the overall efficiency, this leads to higher maximum values of overall efficiency for higher values of ϵ_r as observed in the curves for η. On the contrary, from the bottom panel it is concluded that for higher values of r_p, the overall efficiency gets it maximum value in the region of values of τ where η_h decreases with increasing ϵ_r (the cross point in η_h is now about $\tau = 5.5$, see bottom inset). An so, overall efficiency reaches higher values when decreasing regenerator effectiveness.

Nevertheless, a complete multi-parametric multi-objective analysis for this system, including several compression and expansion stages, to our knowledge, has not been previously presented. Particularly, it will be studied in the next sections an optimization procedure where all the above mentioned parameters are simultaneously considered in the joint optimization of two particular objective functions, the overall plant efficiency, η, and the net power output, P.

3. Multi-objective optimization background

In this section, we briefly introduce some classical concepts about multi-objective optimization, multi-objective evolutionary algorithms and multi-criteria decision-making to help a better understanding of our approach.

3.1. Multi-objective optimization

The Multi-objective Optimization Problem (MOP) can be formally defined as follows[1] [15]:

[1] We are assuming that minimization is the goal of the optimization problem. An equivalent formulation can be defined when the goal is maximization.

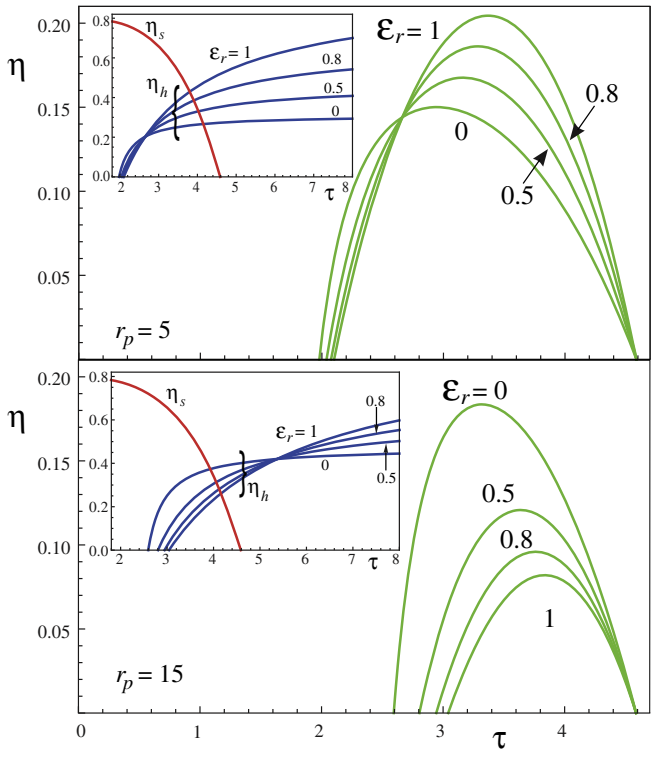

Fig. 2. Behavior of the overall efficiency $\eta = \eta_h \eta_s$, for a simple solar Brayton arrangement ($N_t = N_c = 1$) with the temperature ratio, τ, in terms of the effectiveness recuperator, ϵ_r, for the shown values of r_p [13]. The insets show separately the behavior of the solar collector efficiency, η_s, and of the thermal part, η_h.

$$\begin{aligned} &\text{minimize } f_i(\vec{x}) \quad i = 1,\ldots,q \\ &\text{subject to : } g_k(\vec{x}) \geqslant 0 \quad k = 1,\ldots,m \\ &\qquad\qquad h_l(\vec{x}) = 0 \quad l = 1,\ldots,p \\ &\qquad\qquad x_j^L \leqslant x_j \leqslant x_j^U \quad j = 1,\ldots,n \end{aligned} \tag{7}$$

where $\vec{x} = [x_1, x_2, \ldots, x_n]$ is a solution (a vector of n decision variables), g_k are the m inequalities constraints, h_l are the p equalities constraints, and the variable bounds are the last set of constraints of Eq. (7). The search space $\mathcal{S}$ is defined by the set of solutions that satisfies all the constraints. $F(\vec{x})$ is usually used as a short notation for $[f_1(\vec{x}), \ldots, f_q(\vec{x})]$.

The notion of optimality used in MOP is related to the concept of dominance. A vector $\vec{u} = (u_1, \ldots, u_q)$ dominates another vector $\vec{v} = (v_1, \ldots, v_q)$ if and only if $u_i \leqslant v_i \ \forall i \in 1, \ldots, q$ and there exists at least one j $(1 \leqslant j \leqslant q)$ such that $u_j < v_j$. This is usually notated by $\vec{u} \preceq \vec{v}$. On the other hand, two vectors are non-dominated when none of them dominates the other.

The Pareto Optimal Set (POS) of a given MOP $F(\vec{x})$ is defined as $\mathcal{P}^* = \{\vec{x_1} \in \mathcal{S} | \neg \exists \vec{x_2} \in \mathcal{S}, F(\vec{x_2}) \preceq F(\vec{x_1})\}$. The solutions from the POS satisfy that any two solutions of $\mathcal{P}^*$ are non-dominated with respect to each other, and that any other solution that it does not belong to $\mathcal{P}^*$ must be dominated by at least one member of the set [15]. The representation of the POS in the objective space is known as the Pareto Front. The Pareto Front of a given MOP $F(\vec{x})$ is formally defined as $\mathcal{PF}^* = \{F(\vec{x_1}) | \vec{x_1} \in \mathcal{P}^*\}$.

The solutions from $\mathcal{PF}^*$ represent different trade-offs between the conflicting objectives, *i.e.*, improving the value of one of the objective functions degrades at least one of the other objective functions. As a consequence, and in the absence of further information that would allow to choose among the solutions, all the solutions from $\mathcal{PF}^*$ are equally important. For this reason, when a MOP it is being solved, the solutions not only should be as close as possible to $\mathcal{PF}^*$ (convergence), but also they have to be spread uniformly through $\mathcal{PF}^*$ (diversity).

3.2. Multi-objective evolutionary algorithms

In the first stage of the experimental evaluation, we use a state-of-the-art Multi-Objective Evolutionary Algorithm (MOEA) [15] known as NSGA-II (Nondominated Sorting Genetic Algorithm II) [33]. Evolutionary algorithms (EAs) [34] are stochastic search methods inspired by the natural process of evolution of species. EAs iteratively evolve a population of candidate solutions of the optimization problem guided by a *survival of the fittest* principle. EAs have been widely used for solving MOP since they use a population of solutions which (hopefully) allows to obtain several solutions of the Pareto Optimal Set in a single run. Several EAs have been designed specially for MOP, which are known as MOEAs [15].

The NSGA-II used in the experimental evaluation has been worked out using jMetal [35,36]. jMetal is an object-oriented Java-based framework for MOP with metaheuristic techniques that includes several classical and state-of-the-art algorithms such as NSGA-II, SPEA2 [15] and PAES [15].

3.3. Multi-criteria decision-making

It is important to note that for solving a MOP, besides the search process for finding the non-dominated solutions, there is an explicit decision-making process that is not present in single-objective optimization [15]. It is not enough to find the Pareto Front, but a decision maker, which it is usually an expert in the problem being solved, has to choose one solution from the set. This process is not trivial and involves incorporating additional information, criteria or preferences that are not included in the problem formulation. The different methods used for multi-criteria decision-making can be classified depending on when they incorporate additional information to the decision making process: *a priori*, interactive or *a posteriori*.

In this work, we have followed the *a posteriori* approach that consists in indicating the preferences after the search process. Following this approach, the aim is to find as many Pareto Front solutions as possible and evenly distributed among the front. However, the number of solutions of the front can be large, making impossible to analyze each solution. In this scenario, a subset of the solutions is selected to be analyzed in detail. The criteria for choosing these reference solutions used in this work is described next.

The first points that we include in the subset of solutions analyzed are the extremes of the Pareto Front. These solutions belong to the Pareto Front and minimize one of the objectives ($f_i^* = \arg\min_{\vec{x} \in \mathcal{P}^*} f_i(\vec{x})$). Then, we include solutions from the Pareto Front whose distance is minimal to a given reference point, which is known as the method of compromise programming or the method of global criteria [15]. In this case, the reference point is the ideal point $z^{Ideal} = \left[f_1^*, \ldots, f_q^*\right]$, *i.e.*, the point with the best (minimal) value for each f_i. Since this point does not belong to the Pareto Front, a solution from the Pareto Front is chosen minimizing the distance to the ideal point ($\arg\min_{\vec{x} \in \mathcal{P}^*} d(F(\vec{x}), z^{Ideal})$). The distance can be defined using different norms: we consider the 1-norm distance, Eq. (8), the 2-norm distance or Euclidean distance, Eq. (9), and the infinity norm distance or Chebyshev distance, Eq. (10). As the difference between the magnitudes of the different objective functions could be great, we also consider the three distances normalizing the objective functions between 0 and 1.

$$d_1(F(\vec{x}), z^{Ideal}) = \sum_{i=1}^{q} |f_i(\vec{x}) - z_i^{Ideal}| \tag{8}$$

$$d_2(F(\vec{x}), z^{Ideal}) = \sqrt{\sum_{i=1}^{q} |f_i(\vec{x}) - z_i^{Ideal}|^2} \quad (9)$$

$$d_{\inf}(F(\vec{x}), z^{Ideal}) = \max_{i=1}^{q} |f_i(\vec{x}) - z_i^{Ideal}| \quad (10)$$

4. Experimental evaluation

In this section we formally introduce the optimization problem associated to the solar-driven Brayton cycle. Then, the execution platform is described. Finally, the experimental results obtained are presented and analyzed.

4.1. Problem formulation and experimental settings

The model we have presented in Section 2 is versatile and flexible and, particularly, it can predict the output records of the plant for any value of the design and losses parameters considered. The model was validated in previous works [12,13,25,29]. Also the overall thermodynamic efficiency was optimized by means of an standard thermodynamic optimization procedure in which its maximum value is found in terms of a chosen particular parameter once all the others were previously fixed. In this work, we follow a multi-objective optimization approach (as discussed in Section 3). The purpose from now on is to simultaneously maximize η and $\overline{P}$, that is the adimensional power output, $\overline{P} = P/(C_w T_L)$, in terms, in principle, of all the variables involved in the model.

Table 1 presents the instantiation of our multi-objective optimization problem, including a description of each parameter, the range of possible values and the discretization used. The ranges of possible values of each parameter are realistic and they can be found in [12,13,29,37–41]. The interval of values considered for τ as commented at the end of Section 2 is [2.0,4.4]. All the parameters are taken as independent, so the only constraints in the problem formulation are the ranges considered for each of them, shown in Table 1.

Table 1
Range and discretization of the parameters involved in the multi-objective optimization problem (see text for references and details).

Description	Range	Discretization
Basic design parameters		
Number of compressors	$1 \leqslant N_C \leqslant 5$	1
Number of turbines	$1 \leqslant N_T \leqslant 5$	1
Adiabatic coefficient	$1.35 \leqslant \gamma \leqslant 1.40$	0.01
Overall pressure ratio	$5.00 \leqslant r_p \leqslant 20.00$	1
Heat reservoirs temperature ratio	$2.00 \leqslant \tau \leqslant 4.40$	0.1
Brayton thermal cycle losses parameters		
Irreversibilities coming from the coupling of the working fluid with the heat reservoir at temperature T_L	$0.70 \leqslant \epsilon_H \leqslant 1.00$	0.1
Irreversibilities coming from the coupling of the working fluid with the heat reservoir at temperature T_H	$0.70 \leqslant \epsilon_L \leqslant 1.00$	0.1
Regenerator effectiveness	$0.00 \leqslant \epsilon_r \leqslant 1.00$	0.1
Isentropic efficiency of the compressors	$0.90 \leqslant \epsilon_c \leqslant 0.95$	0.01
Isentropic efficiency of the turbines	$0.90 \leqslant \epsilon_t \leqslant 0.95$	0.01
Pressure drops in the heat input	$0.90 \leqslant \rho_H \leqslant 0.98$	0.02
Pressure drops in the heat release	$0.90 \leqslant \rho_L \leqslant 0.98$	0.02
Heat leakage through the plant to the surroundings	$0.02 \leqslant \xi \leqslant 0.30$	0.04
Solar subsystem losses parameters		
Radiation heat loss coefficient for the solar collector	$0.001 \leqslant M_1 \leqslant 0.003$	0.0001
Convection heat loss coefficient for the solar collector	$0.002 \leqslant M_2 \leqslant 0.010$	0.001
Effective transmittance–absorptance product	$0.70 \leqslant \eta_0 \leqslant 0.90$	0.1

The execution platform is a PC with a Quad Core Intel i7 2600 processor at 3.40 GHz with 16 GB RAM using Linux O.S. The solar-driven Brayton cycle simulation was implemented in Java 1.6.0_22. All the executions were run as single-threaded applications.

4.2. Experimental analysis

The search space of the multi-objective optimization problem associated to the solar-driven Brayton cycle simulation is large. Even using the discretization presented in Section 4.1 the search space has more than $4.31e^{13}$ feasible points. For this reason, we use NSGA-II that is able to make a smart exploration of the search space instead of an exhaustive one.

Taking into account that MOEAs and EAs are stochastic algorithms, 30 independent runs of NSGA-II have been performed. The algorithm was executed for a maximum of 50,000 function evaluations on each run, *i.e.*, we have evaluated only $1.5e^6$ solutions. The algorithm was configured using a population of 100 individuals, the single point crossover [34] with a crossover probability of 0.9, and the bit-flip mutation [34] with a mutation probability of $1/p$, being p the number of parameters of our multi-objective optimization problem. These parameters provide a good compromise between the accuracy of the results and the required execution time.

Since, up to the best of our knowledge, this is the first work that addresses the MOP associated to the multi-step solar-driven Brayton cycle considering simultaneously all the variables detailed in Section 2.2, one of our goals is to find the Pareto Front that is unknown so far. For this reason, we determine a reference Pareto Front combining the non-dominated solutions that resulted from all the runs of NSGA-II and then filtering the non-dominated solutions. It should be noted that since solutions are non-dominated with respect to each other, when combining the output of different runs non-dominated solutions could result dominated. Fig. 3 depicts a flow chart with the sequence of the procedure that was followed. Next we detail the approximated Pareto Front obtained after the first steps.

Fig. 4 presents the Pareto Front obtained using NSGA-II that has 121 non-dominated solutions. The extremes of the Pareto Front are the points with $\overline{P} = 1.0107$ and $\eta = 0.4588$, and $\overline{P} = 2.1627$ and $\eta = 0.3752$. Analyzing the Pareto Optimal Set (the solutions of the Pareto Front in the domain space), we have found that 13 out of the 16 parameters of our model are fixed in all the solutions. The parameters that are fixed are those labelled as *I-conf*. in Table 2. Most fixed parameters are associated to losses (see Table 1). They reach the highest value for the interval considered (efficiencies or effectivenesses) or the lowest one (losses parameters themselves). The number of turbines and compressors, N_c and N_t, reach the highest value that was taken: $N_t = N_c \equiv N = 5$. So, the variables that really offer diverse combinations at the Pareto Front are the design parameters r_p, γ, and τ.

Since only r_p, γ, and τ parameters take different values for the solutions of the Pareto Front obtained, and in order to find the best possible approximation to the real Pareto Front as an input for the decision-making process, we implement an exact algorithm that enumerates all possible solutions varying the values for the parameters r_p, γ, and τ (in the same intervals that in Table 1), and keeping fixed the rest of the parameters (this is called *I-conf*. in Table 2). We stress here that the consideration of γ as optimization parameter is equivalent to analyze different working fluids, because in our Brayton heat engine the working fluid is an ideal gas with

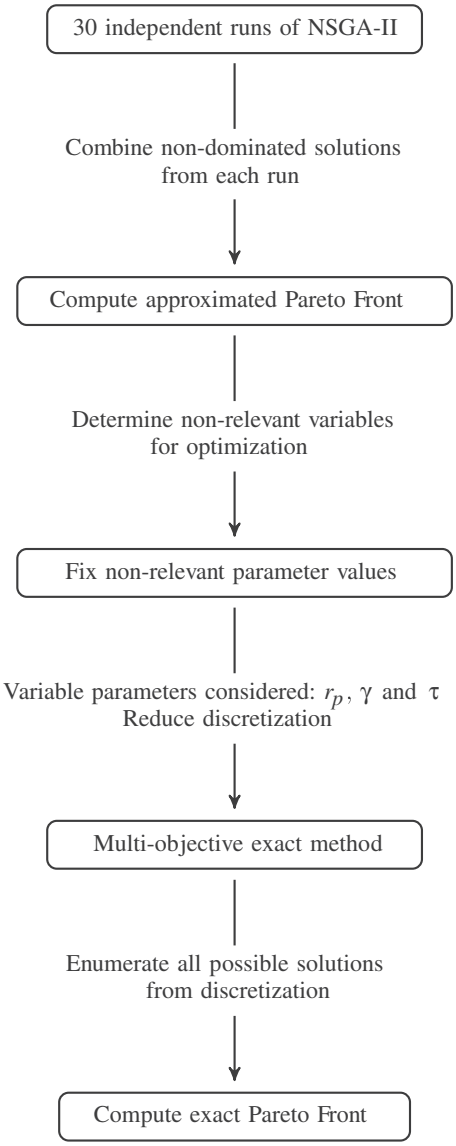

Fig. 3. Flow chart scheme with the sequence of operations developed in the optimization procedure.

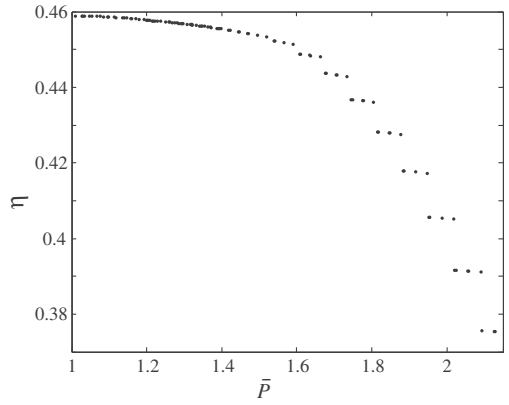

Fig. 4. Pareto Front obtained using the algorithm NSGA-II and allowing the simultaneous variation of all the parameters.

Table 2
Losses parameters in the different configurations considered. The *I-conf.* is that obtained by means of the NSGA-II algorithm allowing losses parameters fluctuate up to ideal values. The *R-conf.* one is taken by considering realistic values for those losses parameters. The *NRR-conf.* is the real non-regenerative case.

Parameter	*I-conf.*	*R-conf.*	*NRR-conf.*
ϵ_H	1.0	0.9	0.9
ϵ_L	1.0	1.0	1.0
ϵ_r	1.0	0.85	0.0
ϵ_c	0.95	0.84	0.84
ϵ_t	0.95	0.89	0.89
ρ_H	0.98	0.98	0.98
ρ_L	0.98	0.98	0.98
ξ	0.02	0.02	0.02
M_1	0.001	2.25×10^{-3}	2.25×10^{-3}
M_2	0.002	2.5×10^{-3}	2.5×10^{-3}
η_0	0.9	0.8	0.8

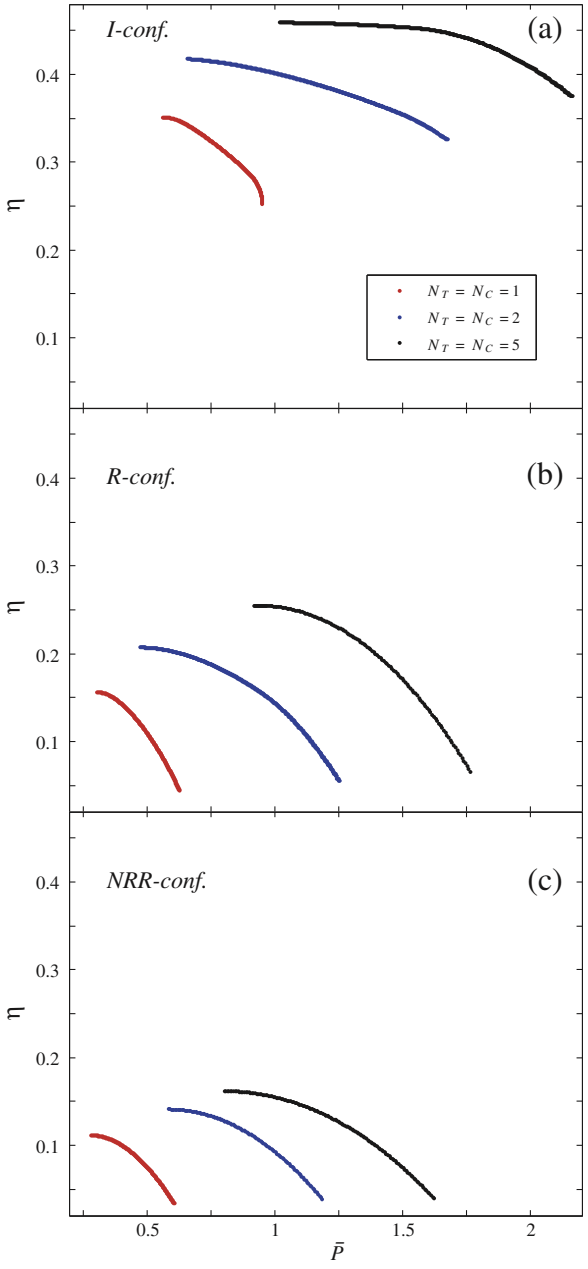

Fig. 5. Pareto Fronts obtained using an exact method by considering as free parameters r_p, γ, and τ with $N = 1$, 2, and 5. The rest of parameters are those contained in Table 2: (a) *I-conf.*; (b) *R-conf.*; and (c) *NRR-conf.*

Table 3
Subset of solutions analyzed from the Pareto Front for the *I-conf*. with a number of compression–expansion stages $N = 1, 2$, and 5. In each case it is shown in parenthesis the number of points of the front.

$\overline{P}$	η	r_p	γ	τ
$N = 1$ (7796)				
0.5616	0.3510	5.0	1.350	3.71
0.8010	0.3126	6.40	1.364	4.25
0.8049	0.3117	6.80	1.353	4.25
0.8406	0.3029	7.0	1.363	4.31
0.8905	0.2897	7.9	1.359	4.39
0.9218	0.2794	9.3	1.361	4.40
0.9453	0.2653	11.8	1.361	4.40
0.9518	0.2518	14.6	1.360	4.40
$N = 2$ (7444)				
0.6569	0.4175	5.0	1.350	3.51
1.2054	0.3848	12.4	1.389	3.90
1.2496	0.3808	16.0	1.357	3.93
1.2585	0.3799	16.0	1.359	3.94
1.5986	0.3399	20.0	1.400	4.28
1.6559	0.3295	20.0	1.400	4.37
1.6750	0.3256	20.0	1.400	4.40
$N = 5$ (15,638)				
1.0185	0.4588	8.6	1.376	3.40
1.7052	0.4451	20.0	1.400	3.76
1.7838	0.4383	20.0	1.400	3.87
1.8208	0.4338	20.0	1.398	3.93
2.0951	0.3896	20.0	1.399	4.31
2.1413	0.3802	20.0	1.400	4.37
2.1627	0.3752	20.0	1.400	4.40

Table 4
Subset of solutions analyzed from the Pareto Front for the *R-conf*. with $N = 1, 2$, and 5. In each case it is shown in parenthesis the number of points of the front.

$\overline{P}$	η	r_p	γ	τ
$N = 1$ (20,190)				
0.3044	0.1562	5.0	1.350	3.41
0.4594	0.1254	5.6	1.377	3.92
0.4905	0.1139	6.3	1.363	4.01
0.4976	0.1111	5.8	1.392	4.03
0.5566	0.0844	6.4	1.395	4.20
0.5818	0.0714	7.3	1.376	4.27
0.6282	0.0448	7.4	1.400	4.40
0.6284	0.0445	8.6	1.369	4.40
$N = 2$ (23,162)				
0.4737	0.2071	6.9	1.355	3.22
0.9382	0.1573	20.0	1.396	3.85
0.9573	0.1535	20.0	1.400	3.88
0.9676	0.1513	20.0	1.398	3.90
1.1456	0.1000	20.0	1.400	4.21
1.2026	0.0778	20.0	1.400	4.31
1.2540	0.0552	20.0	1.400	4.40
$N = 5$ (276)				
0.9184	0.2549	20.0	1.390	3.12
1.3548	0.2092	20.0	1.400	3.77
1.4264	0.1917	20.0	1.400	3.88
1.4524	0.1846	20.0	1.400	3.92
1.6346	0.1231	20.0	1.400	4.20
1.6931	0.0986	20.0	1.400	4.29
1.7647	0.0654	20.0	1.400	4.40

temperature independent adiabatic constant, γ. So, γ represents the mean adiabatic constant of the considered working fluid in the interval of temperatures experienced in the cycle. The analysis of an optimal range for γ should be considered as a guide for searching an adequate working gas, in which refers to its adiabatic coefficient. Particularly, Tournier et al. [42] presented a nice review of the properties of noble gases and binary mixtures for closed Brayton applications.

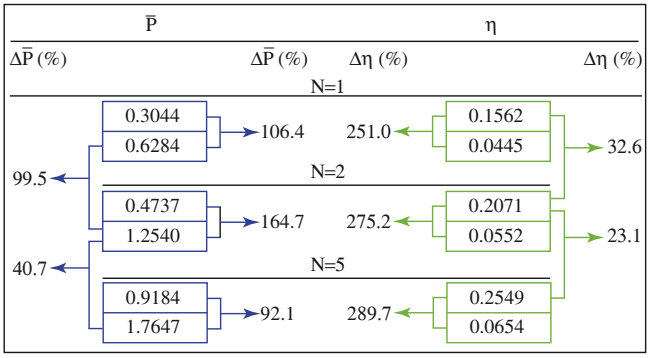

Fig. 6. Relative increments of power output, $\Delta\overline{P}$, and overall efficiency, $\Delta\eta$, between the extremes of the Pareto Front for the R configuration and the number of compression–expansion stages considered, N. All the percentages are calculated with respect to the lowest value in each case. The scheme also shows the increase of $\overline{P}$ and η with N.

Table 5
Subset of solutions analyzed from the Pareto Front for the *NRR-conf*. with $N = 1, 2$, and 5. In each case it is shown in parenthesis the number of points of the front.

$\overline{P}$	η	r_p	γ	τ
$N = 1$ (33,042)				
0.2820	0.1113	9.7	1.357	3.45
0.4437	0.0912	8.8	1.390	3.93
0.4714	0.0840	10.1	1.359	4.01
0.4814	0.0812	8.8	1.393	4.04
0.5527	0.0568	10.9	1.358	4.25
0.5788	0.0463	8.9	1.395	4.32
0.6072	0.0337	9.0	1.388	4.40
0.6073	0.0335	8.5	1.396	4.40
$N = 2$ (113)				
0.5853	0.1409	20.0	1.400	3.28
0.8911	0.1147	20.0	1.400	3.85
0.9394	0.1057	20.0	1.400	3.94
0.9555	0.1025	20.0	1.400	3.97
1.1110	0.0630	20.0	1.400	4.26
1.1540	0.0495	20.0	1.400	4.34
1.1861	0.0386	20.0	1.400	4.40
$N = 5$ (137)				
0.8028	0.1616	20.0	1.400	3.04
1.2247	0.1305	20.0	1.400	3.74
1.2910	0.1197	20.0	1.400	3.85
1.3151	0.1154	20.0	1.400	3.89
1.5321	0.0658	20.0	1.400	4.25
1.5864	0.0502	20.0	1.400	4.34
1.6225	0.0390	20.0	1.400	4.40

In this case, the search space is relatively small (2400 feasible points), the discretizations were reduced one order of magnitude with respect to those in Table 1, *i.e.*, the step is 0.1 for r_p, 0.001 for γ, and 0.01 for τ, resulting a search space with more than 1.85e^6 points. We performed the calculations for three different values of N ($N = 1, 2$, and 5).

Fig. 5(a) presents the Pareto Fronts obtained using the exact method for the *I-conf*. These Pareto Fronts are more dense than the previous one (Fig. 4), and are composed between 7444 ($N = 2$) and 15,638 ($N = 5$) non-dominated solutions. The extremes of the Pareto Front for $N = 1$ are the points ($\overline{P} = 0.5616, \eta = 0.3510$) and ($\overline{P} = 0.9518, \eta = 0.2518$) and for the highest number of compression–expansion stages, $N = 5$, ($\overline{P} = 1.0185, \eta = 0.4588$) (this solution dominates the extreme of the first Pareto Front obtained, Fig. 4), and ($\overline{P} = 2.1627$, $\eta = 0.3752$). In Fig. 5(a) it appears clear the increase both in power output and efficiency when multiplying the number of stages from

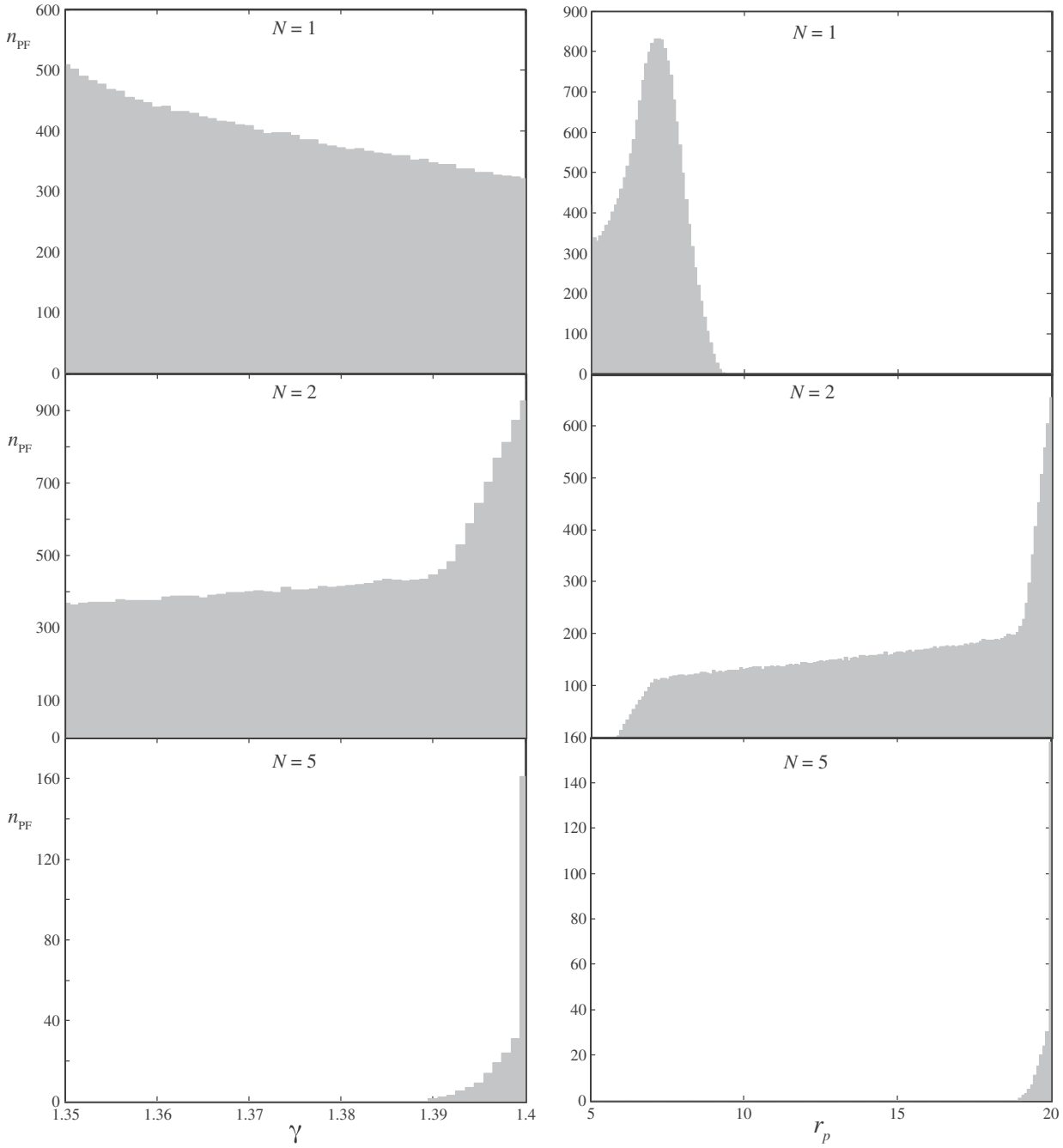

Fig. 7. Number of non-dominated points of the Pareto Front, n_{PF}, with given values of γ and r_p for the *R-conf*. The discretization considered and the intervals for the parameters are those in Tables 1 and 2.

the single stage Brayton case to $N = 5$. In real plants is nowadays considered unpractical a larger number of compression–expansion stages, mainly because of economical reasons [43,44].

After obtaining the Pareto Front of the MOP associated to the solar-driven Brayton cycle, we conduct the decision-making process. Table 3 presents the subset of solutions analyzed from the Pareto Front. This subset was selected using the criteria presented in Section 3.3. At sight of the table it could be concluded that for $N = 1$ small pressure ratios (r_p around 5–7) would be required to get high efficiencies and relatively low power output. On the opposite the highest power outputs are obtained at r_p around 12–14. When the number of stages increases, we note that globally r_p at the Pareto Front also increases, but only up to a saturation value around 20. These results on the r_p values for the Pareto Front non-dominated points are in accordance with previous results from single optimization procedures, where all the rest of variables were considered as fixed and the only optimization parameter was r_p [12,13]. We shall see later on the effects of widening the considered interval of values for r_p as well as that for γ.

With respect to the influence of the adiabatic constant γ, its values at the Pareto Front globally increase when increasing the number of compression–expansion steps. Note that in our theoretical model γ is taken as temperature independent and thus, should be considered as an average value between the extreme temperatures in the cycle. The values of the temperature ratio, τ, have a clear tendency: they are always lower for those non-dominated

points with high overall efficiencies. This is reasonable because overall efficiency is proportional to the solar collector efficiency which decreases with the temperature ratio, as the heat losses increase. On the contrary, the combination of parameters leading to high power output are those with high temperature ratios, and so, high turbine inlet temperatures. The lowest value of τ ($\tau = 3.40$) is obtained for $N = 5$ and the highest efficiency, that for instance for an external temperature of 288 K corresponds to a working temperature for the collector of 979 K. On the other side, the highest value of τ is $\tau = 4.40$ that would lead to a collector temperature of 1267 K. Temperatures close to these ones are nowadays feasible since have been reported in several experimental facilities and prototype plants [3,45].

As mentioned before, the results of Fig. 5(a) and Table 3 were obtained by taking all the losses in the system at their minimum values, within the intervals considered in Table 1. The Pareto Front was also calculated for a realistic set of losses parameters. This set is labelled *R-conf*. in Table 2. These values were taken from several references, [25,37,38,40,41,46–48]. The corresponding Pareto Fronts and the subsets of solutions are contained in Fig. 5(b) and Table 4. In general, there is a clear decrease both in power output and overall efficiency with respect to the case *I-conf*., because now the losses are greater and closer to the real ones in existing facilities. Nevertheless, the comments above about the values and evolution of the design parameters r_p, γ, and τ are still valid now. Probably, the main difference when comparing the values of r_p in Tables 3 and 4 is that for $N = 1$ smaller values of r_p are required in the realistic configuration, *R-conf*., when comparing with the ideal one, *I-conf*. The results in Tables 3 and 4 suggest that a broadening in the intervals considered for r_p and γ could affect the results. These effects will be detailed below in this section. The interval considered for τ is not susceptible to be enlarged because negative values of efficiency would appear as it was explained from Fig. 2.

In Fig. 6 the relative variations of power output, $\Delta\overline{P}$ and overall efficiency, η, between the extreme values of the Pareto Fronts for the *R-conf*. are depicted. For instance, for $N = 1$ the relative increase in $\overline{P}$ amounts 1.06 and in η, the corresponding increase is 2.51. When comparing the increase in the maximum achievable power output between different configurations with a different number of stages increments are quite diverse: for power output when going from $N = 1$ to $N = 2, \Delta\overline{P} = 0.99$ while $\Delta\eta = 0.33$. When increasing the number of steps from 2 to 5 the increasings are not very large, $\Delta\overline{P} = 0.41$ and $\Delta\eta = 0.23$. As a general conclusion, there is a wide interval in the power output and in the overall efficiency obtained from the plant in terms of the basic design parameters considered, pressure and temperature ratios, adiabatic constant of the working fluid, and number of compression–expansion stages. In other words a rigorous optimization analysis of the plant, at the design stage, is required to obtain good output records, and so to estimate the economical viability of the installation.

We have also analyzed the influence of the regenerator in the optimization process of the plant by constructing the Pareto Fronts with the same parameters that in the so-called *R-conf*., but eliminating the recuperator, that in our model is identical to fixing its effectiveness equal to zero. This configuration is named *NRR-conf*. in Table 2. The associated Pareto Fronts and the set of analyzed points are represented in Fig. 5(c) and Table 5. The decrease of the overall efficiency, is clear when comparing with the results for the recuperative plant (Fig. 5(b) and Table 4). For $N = 1$ the decrease for the highest efficiency point amounts approximately 40%, for $N = 2$, 47%, and for $N = 5$, 58%. With respect to the power output, the absence or presence of a regenerator in the plant design should be indifferent, because regeneration

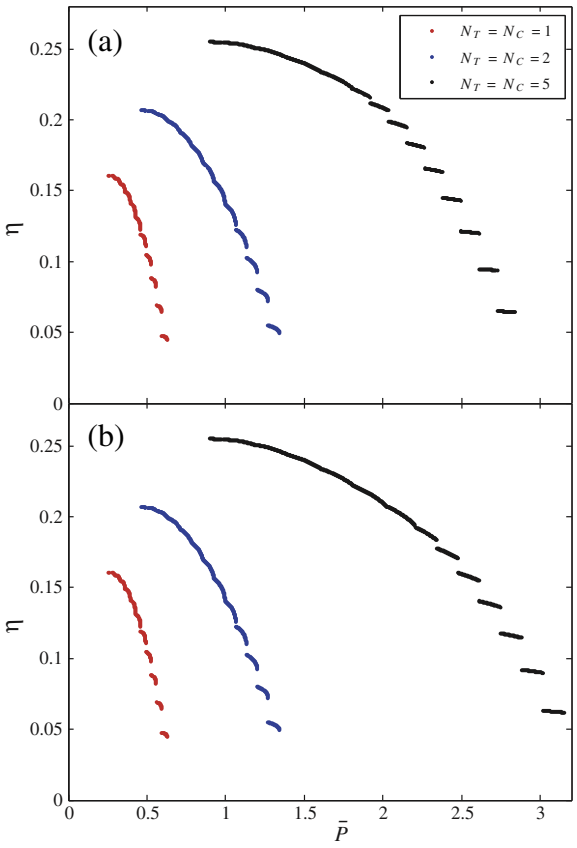

Fig. 8. Pareto Fronts obtained for the *R-conf*. with the exact method and considering wide intervals for γ and r_p. (a) γ varies between 1.2 and 1.7 and r_p between 5 and 50. (b) γ varies between 1.2 and 1.8 and r_p between 5 and 80. Note specially that in the bottom figure and $N = 5$ power output values reach higher values.

Table 6
Subset of solutions analyzed from the Pareto Front for the *R-conf*. with $N = 2$, and 5 for the following intervals of γ and r_p. $N = 2 : \gamma \in [1.2,1.7]$, $r_p \in [5,50]$. $N = 5 : \gamma \in [1.2,1.8]$, $r_p \in [5,80]$. Note the differences with the solutions of Table 4, specially in the values of $\overline{P}$ for $N = 5$.

$\overline{P}$	η	r_p	γ	τ
$N = 2$ (6136)				
0.4650	0.2070	10	1.28	3.2
0.9007	0.1644	21	1.37	3.8
0.9751	0.1499	37	1.32	3.9
0.9929	0.1443	19	1.48	3.9
1.2141	0.0794	39	1.32	4.3
1.2695	0.0732	17	1.62	4.1
1.3415	0.0497	19	1.62	4.4
1.3417	0.0494	47	1.42	4.4
$N = 5$ (276)				
0.9017	0.2549	10	1.57	3.1
2.3320	0.1844	79	1.79	3.8
2.3354	0.1841	78	1.80	3.8
2.3378	0.1839	79	1.80	3.8
2.9887	0.0903	78	1.78	4.3
3.1475	0.0618	79	1.80	4.4
3.1518	0.0618	80	1.80	4.4

is an internal heat transfer effect, that does not affect the net power output. This is corroborated by comparing the columns relative to $\overline{P}$ in Tables 4 and 5. The differences in between should be ascribed to the discretization process performed to obtain the Pareto Fronts. In reference to the optimum values of the design parameters that lead to the Pareto Fronts, the values of τ in both tables are very

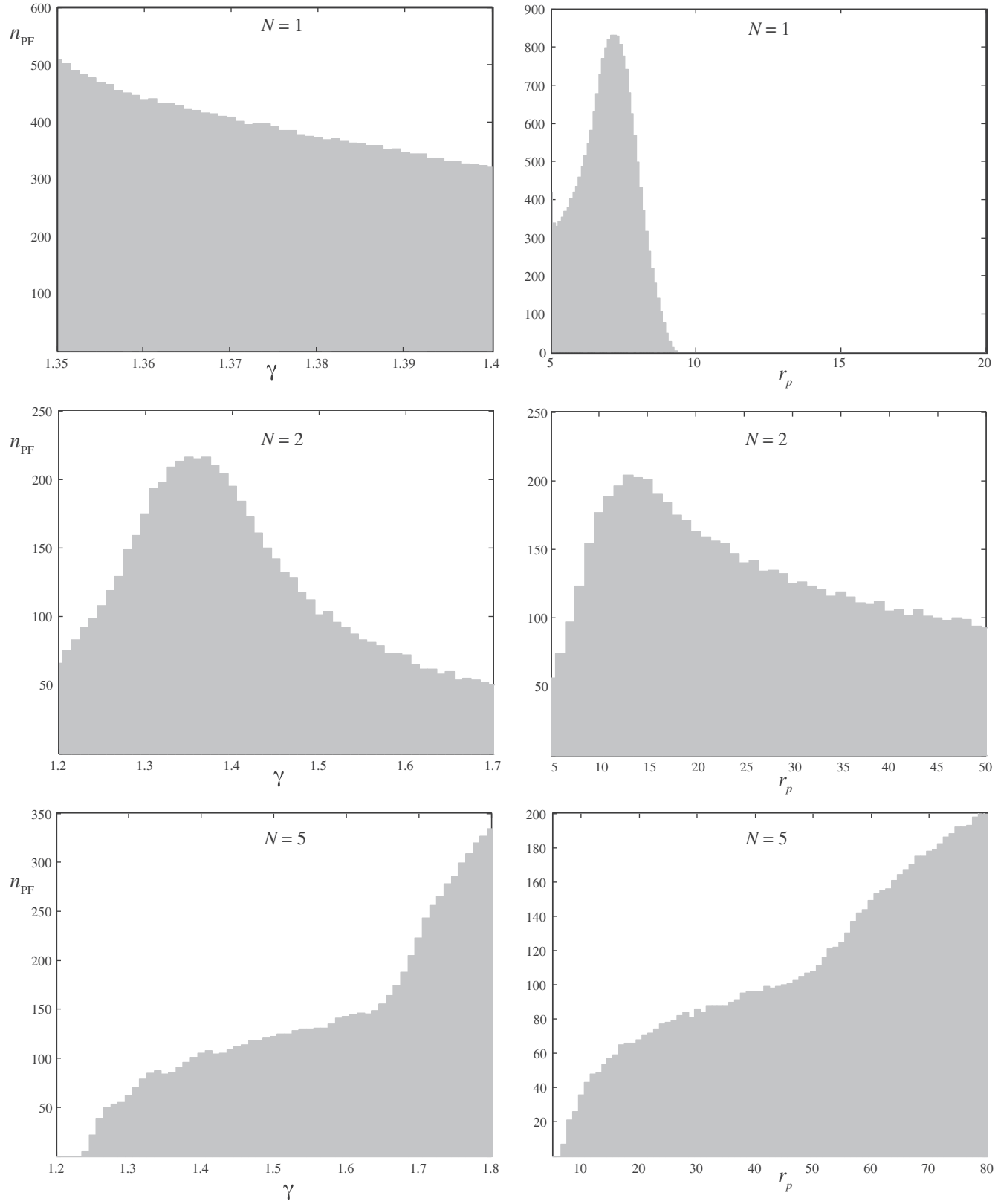

Fig. 9. Histograms of the number Pareto Front points, n_{PF}, obtained with the exact method for the *R-conf*. and considering wide intervals for γ and r_p in the cases $N = 2$ and $N = 5$.

similar, so the existence of a regenerator does not influence the optimum working temperature of the solar collector. Opposite, pressure ratios for $N = 1$, clearly change. They are larger in the case of no regeneration. For the *R-conf*., r_p in the subset of the Pareto Front analyzed is in the interval $[5.0, 8.6]$, but in the *NRR-conf*. the interval is $[8.5, 10.9]$. The values of γ are similar in both

configurations: oscillate between 1.35 and 1.4 for $N = 1$ and tend to reach the highest value, 1.4, for more compression–expansion steps.

We finish this section by analyzing the effects of the intervals considered for γ and r_p in the Pareto Fronts. In Fig. 7 we show the histograms of the number of points of the Pareto Fronts with given values of γ and r_p, n_{PF}, for the *R-conf.* (the intervals for the parameters are those in Table 1). For $N = 2$ and $N = 5$ the plots suggest that probably wider intervals for both parameters will lead to more non-dominated points (because distributions are not bell-shaped), and so, broader intervals could lead to different Pareto Fronts. In Fig. 8 and Table 6 we show the Pareto Fronts calculated with wider intervals both for γ and r_p, and the corresponding subset of solutions analyzed. The particular intervals considered are shown in the figure. The most important effect is that wider intervals provoke a displacement of the power output for $N = 5$ to higher values. For $N = 1$ and $N = 2$ the shape of the fronts and their numerical values are similar to those of Fig. 5(b) with narrower intervals.

Fig. 9 represents n_{PF} as functions of γ and r_p for wide intervals. For $N = 2$ the distributions show a maximum: around 1.35 for γ and around 13 for r_p. Nevertheless, when increasing the number of stages to $N = 5$, the distributions monotonically increase, without displaying a maximum. Even broader intervals in this case would be unphysical. In particular, the behavior with r_p is in accordance with previous results (see Fig. 6 in [25] and Fig. 5 in [12]). In those works the power and the efficiency for a similar system were independently optimized with a thermodynamic single-objective procedure. It was concluded that both objective functions show a maximum with r_p for values of N below 2, but for a higher number of intermediate stages, power and efficiency monotonically increase with r_p, *i.e.*, do not have a maximum in terms of r_p, that is precisely what could be concluded from the bottom right panel of Fig. 9.

5. Conclusions

In this work a multi-objective optimization analysis of a multi-step regenerative Brayton thermosolar plant was performed. At difference with previous works [24], the analysis explicitly considers several compression and expansion stages and, in principle, all the variables of the system (from the solar subsystem and the thermodynamic engine) are independently checked in order to discriminate the most important ones in regards to the overall plant efficiency and power output.

In a first stage, the Pareto Front of the system was obtained by means of a NSGA-II algorithm allowing fluctuations in all the parameters, both design parameters as pressure and temperature ratios (r_p and τ respectively), the average adiabatic constant of the working gas (γ), and the number of compression–expansion stages (N) with reasonable limits for all the parameters, and also losses parameters arising from the thermal engine itself and from the solar subsystem. This procedure involved 15 different parameters with appropriate discretization for each. The objective functions selected were the overall thermodynamic efficiency of the system (η) and the dimensional power output ($\overline{P}$). It is important to note that in a system like the one considered, in which the input energy, solar energy, is free (fuel is not included in the operation costs) the thermal efficiency represents the power obtained for a certain size of the solar collector arrangement. The solar plant has costs associated to construction investment and also to maintenance, so an optimum thermal efficiency represents a good compromise between power output and solar plant investing.

The analysis of the obtained Pareto Front revealed that no intriguing coupling effects occurred and all the losses parameters reached their corresponding minimum values for the non-dominated points. Thus, we restricted our study to design parameters and recalculated the Pareto Front by means of exact meshed computations with a fine grid. Subsets of the calculated Pareto Front were selected and analyzed after following a multi-criteria decision making process.

It was shown that in any case the variations of efficiency and power output associated to the design points in the Pareto Front are important, *i.e.*, small changes in r_p, τ, and γ lead to quite different values of η and $\overline{P}$. This reinforces the idea that in the design of this type of plants a previous basic optimization study is basic in order to find the appropriate numerical intervals of the main thermodynamic design variables. Specially elucidating are the conclusions with respect to the pressure ratio values of the non-dominated points at the Pareto Fronts. The analysis presented concludes that for mono-stage plants, $N = 1$, with realistic irreversibility parameters, the pressure ratio should be between approximately 5 and 9. The distribution of the number of non-dominated points displays a maximum at approximately $r_p = 7.5$. For plants with $N = 2$ the distribution is centered around $r_p = 15$, *i.e.*, there is some kind or multiplicative effect. But for $N = 5$, the distribution is a monotonically increasing function. This is in accordance with previous single-objective thermodynamic optimization procedures which showed that the efficiency and power output for high enough values of N are monotonic functions of r_p and do not display maximum values [12,25].

In summary, the systematic multi-objective and multi-parametric optimization of a pure solar-driven plant considered shows the wide interval of optimization possibilities of these plants when electing as objective functions their overall performance and power output. This kind of studies at an initial design stage of the plant are very elucidating to decide the main thermodynamic plant parameters. Small changes in those parameters could lead to an undesired design point with important misplacements of those output records.

Acknowledgements

M. Pedemonte, P. Ezzatti, and P.L. Curto-Risso acknowledge support from Universidad de la República and Agencia Nacional de Investigación e Innovación, Uruguay. M. Pedemonte and P. Ezzatti also thank support from Programa de Desarrollo de las Ciencias Básicas, Uruguay. A. Medina, A. Calvo Hernández, and S. Sánchez Orgaz acknowledge financial support from MINECO of Spain, Grant ENE2013-40644-R, and Universidad de Salamanca. S. Sánchez Orgaz also wish to thank to Banco Santander of Spain for financial support in her visit to Montevideo.

References

[1] SOLGATE. Solar hybrid gas turbine electric power system. Tech rep EUR 21615, European Commission; 2005.
[2] Solar-hybrid power and cogeneration plants. Tech rep, European Commission; 2011. <ordis.europa.eu/publication/rcn/13318_en.html>.
[3] R. Korzynietz, M. Quero, R. Uhlig, SOLUGAS-future solar hybrid technology. Tech rep, SolarPaces; 2012. <http://cms.solarpaces2012.org/proceedings/paper/7ee7e32ece8f2f8e0984d5ebff9d77b>.
[4] Koyun A. Performance analysis of a solar-driven heat engine with external irreversibilities under maximum power and power density condition. Energy Convers Manage 2004;45:1941–7.
[5] Blank D, Wu C. Finite-time power limit for solar-radiant Ericsson engines in space applications. Appl Therm Eng 1998;18:1347–57.
[6] Kaushik SC, Kumar S. Finite time thermodynamic evaluation of irreversible Ericsson and Stirling heat engines. Energy Convers Manage 2001;42:295–312.
[7] Zhang Y, Lin B, Chen J. Optimum performance characteristics of an irreversible solar-driven Brayton heat engine at the maximum overall efficiency. Renew Energy 2007;32:856–67.
[8] Al-Sood M, Matrawy K, Abdel-Rahim Y. Optimum parametric performance characterization of an irreversible gas turbine Brayton cycle. Int J Energy Environ Eng 2013;4:37.

[9] Haseli Y. Optimization of a regenerative Brayton cycle by maximization of a newly defined second law efficiency. Energy Convers Manage 2013;68:133–40.
[10] Le Roux W, Bello-Ochende TMJ. A review on the thermodynamic optimisation and model of the solar thermal Brayton cycle. Renew Sust Energy Rev 2013;28:677–90.
[11] Spelling J, Favrat D, Martin A, Augsburger G. Thermoeconomic optimization of a combined-cycle solar tower plant. Energy 2012;41:113–20.
[12] Sánchez-Orgaz S, Medina A, Calvo Hernández A. Maximum overall efficiency for a solar-driven gas turbine power plants. Int J Energy Res 2013;37:1580–91.
[13] Sánchez-Orgaz S, Medina A, Calvo Hernández A. Recuperative solar-driven multi-step gas turbine power plants. Energy Convers Manage 2013;67:171–8.
[14] Olivenza-León D, Medina A, Calvo Hernández A. Thermodynamic modeling of a hybrid solar gas-turbine power plant. Energy Convers Manage 2015;93:435–47.
[15] Deb K. Multi-objective optimization using evolutionary algorithms. New York (NY, USA): John Wiley & Sons, Inc.; 2001.
[16] Ahmadi M, Hossseinzade H, Sayyaadi H, Sayyadi A, Kimiaghalam F. Application of the multi-objective optimization method for designing a powered Stirling heat engine: design with maximized power, thermal efficiency and minimized pressure loss. Renew Energy 2013;60:313–22.
[17] Ahmadi M, Sayyaadi H, Dehghani S, Hosseinzade H. Designing a solar powered stirling heat engine based on multiple criteria: maximized thermal efficiency and power. Energy Convers Manage 2013;75:282–91.
[18] Ahmadi M, Ahmadi M. Thermodynamic analysis and optimization of an irreversible Ericsson cryogenic refrigerator cycle. Energy Convers Manage 2015;89:147–55.
[19] Besarati S, Atashkari K, Jamali A, Hajiloo A, Nariman-zadeh N. Multi-objective thermodynamic optimization of combined Brayton and inverse Brayton cycles using genetic algorithms. Energy Convers Manage 2010;51:212–7.
[20] Avval H, Ahmadi P, Ghaffarizadeh A, Saidi M. Thermo-economic–environmental multiobjective optimization of a gas turbine power plant with preheater using evolutionary algorithm. Int J Energy Res 2011;35:389–403.
[21] Le Roux W, Bello-Ochende TMJ. The efficiency of an open-cavity tubular solar receiver for a small-scale solar thermal Brayton cycle. Energy Convers Manage 2014;84:457–70.
[22] Li Y, Liao S, Liu G. Thermo-economic multi-objective optimization for a solar-dish Brayton system using NSGA-II and decision making. Electr Power Energy Syst 2015;64:167–75.
[23] Sadatsakkak S, Ahmadi M, Bayat R, Pourkiaei S, Feidt M. Optimization density power and thermal efficiency of an endoreversible Braysson cycle by using non-dominated sorting genetic algorithm. Energy Convers Manage 2015;93:31–9.
[24] Ahmadi M, Ahmadi M, Feidt M. Performance optimization of a solar-driven multi-step irreversible Brayton cycle based on a multi-objective genetic algorithm. Oil Gas Sci Technol <http://dx.doi.org/10.2516/ogst/2014028>.
[25] Sánchez-Orgaz S, Medina A, Calvo Hernández A. Thermodynamic model and optimization of a multi-step irreversible Brayton cycle. Energy Convers Manage 2010;51:2134–43.
[26] Duffie J, Beckman W. Solar engineering of thermal processes. Hoboken (New Jersey): John Wiley and Sons; 2006.
[27] Gordon JM. On optimized solar-driven heat engines. Sol Energy 1988;40:457–61.
[28] Kandpal T, Singhl A, Mathur S. Optimum power from a solar thermal power plant using solar concentrators. Energy Convers Manage 1983;23:103–6.
[29] Sánchez-Orgaz S. Model, analysis, and thermodynamic optimization of Brayton multi-step power plants. Application to thermosolar plants, Ph.D. thesis, Universidad de Salamanca, Spain; 2012. <http://gtfe.usal.es/Eng/>.
[30] Sahin B, Kodal A, Yilmaz T, Yavuz Y. Maximum power density analysis of an irreversible Joule–Brayton engine. J Phys D: Appl Phys 1996;29:1162–7.
[31] Bejan A. Advanced engineering thermodynamics. 3rd ed. Hoboken (New Jersey): Wiley; 2006.
[32] Ust Y, Sogut OS, Sahin B, Durmayaz A. Ecological coefficient of performance (ECOP) optimization for an irreversible heat engine with variable-temperature heat reservoirs. J Energy Inst 2006;79:47–52.
[33] Deb K, Pratap A, Agarwal S, Meyarivan T. A fast and elitist multiobjective genetic algorithm: NSGA-II. IEEE Trans Evol Comput 2002;6(2):182–97.
[34] Goldberg D. Genetic algorithms in search, optimization, and machine learning. Addison-Wesley; 1989.
[35] Durillo J, Nebro A, Alba E. The jMetal framework for multi-objective optimization: design and architecture. In: CEC 2010, Barcelona, Spain; 2010. p. 4138–325.
[36] Durillo JJ, Nebro AJ. jMetal: a java framework for multi-objective optimization. Adv Eng Softw 2011;42(10):760–71.
[37] Wu L, Lin G, Chen J. Parametric optimization of a solar-driven Braysson heat engine with variable heat capacity of the working fluid and radiation–convection heat losses. Renew Energy 2010;35:95–100.
[38] Roco JMM, Velasco S, Medina A, Calvo Hernández A. Optimum performance of a regenerative Brayton thermal cycle. J Appl Phys 1997;82:2735–41.
[39] Chen L, Wang J, Sun F. Power density analysis and optimization of an irreversible closed intercooled regenerated Brayton cycle. Math Comput Model 2008;48:527–40.
[40] Herrera C, Sandoval J, Rosillo M. Power and entropy generation of an extended irreversible Brayton cycle: optimal parameters and performance. J Phys D: Appl Phys 2006;39:3414–24.
[41] de Mello P, Monteiro D. Thermodynamic study of an EFGT (Externally fired gas-turbine) cycle with one detailed model for the ceramic heat exchanger. In: Proceedings of ECOS 2011 conference, Novi Sad, Serbia; 2011.
[42] Tournier J-MP, El-Genk M. Properties of noble gases and binary mixtures for closed Brayton cycle applications. Energy Convers Manage 2008;49:469–92.
[43] Horlock J. Cogeneration-combined heat and power plants. Krieger; 1997.
[44] Horlock J. Advanced gas turbine cycles. Oxford: Pergamon; 2003.
[45] Heller P, Pfänder M, Denk T, Tellez F, Valverde A, Fernández J, et al. Test and evaluation of a solar powered gas turbine system. Sol Energy 2006;80:1225–30.
[46] Calvo Hernández A, Roco JMM, Medina A. Power and efficiency in a regenerative gas-turbine with multiple reheating and intercooling stages. J Phys D: Appl Phys 1996;29:1462–8.
[47] Kautz M, Hansen U. The externally fired gas turbine (EFGT-cycle) and simulation of the key components. Appl Energy 2007;84:795–805.
[48] Galanti L, Massardo A. Micro gas turbine thermodynamic and economic analysis up to 500 kWe. Appl Energy 2011;88:4795–802.